

Article

Fixed-Target Pink-Beam Serial Synchrotron Crystallography at Pohang Light Source II

Yongsam Kim ¹ and Ki Hyun Nam ^{2,*} 

¹ Pohang Accelerator Laboratory, Pohang University of Science and Technology, Pohang 37673, Republic of Korea

² College of General Education, Kookmin University, Seoul 02707, Republic of Korea

* Correspondence: structure@kookmin.ac.kr

Abstract: Serial crystallography (SX) enables the determination of the structure of macromolecules or small molecules with minimal radiation damage. In particular, biomolecule structures determined using the SX technique have the advantage of providing room-temperature crystal structures with high biological relevance. The SX technique requires numerous crystals to be collected to complete three-dimensional structural information. To minimize crystal sample consumption, we introduced SX data collection with fixed-target (FT) pink-beam serial synchrotron crystallography (SSX) at the 1C beamline of Pohang Light Source II. A new sample holder consisting of a magnetic frame with a nylon mesh was developed for easy sample handling. The FT-pink-SSX diffraction data were collected by continuously scanning X-rays using a stepping motor. The room-temperature structures of glucose isomerase and lysozyme were successfully determined at a resolution of 1.7 and 2.2 Å, respectively. The use of pink-beam FT-SSX in experimental applications and data acquisition for large beam sizes is discussed. Our results provide useful information for future pink-beam SSX and SX data collection using large X-ray beams.

Keywords: serial crystallography; pink-beam; fixed-target scanning; room-temperature; synchrotron



Citation: Kim, Y.; Nam, K.H. Fixed-Target Pink-Beam Serial Synchrotron Crystallography at Pohang Light Source II. *Crystals* **2023**, *13*, 1544. <https://doi.org/10.3390/cryst13111544>

Academic Editor: Borislav Angelov

Received: 19 September 2023

Revised: 9 October 2023

Accepted: 26 October 2023

Published: 27 October 2023



Copyright: © 2023 by the authors. Licensee MDPI, Basel, Switzerland. This article is an open access article distributed under the terms and conditions of the Creative Commons Attribution (CC BY) license (<https://creativecommons.org/licenses/by/4.0/>).

1. Introduction

Serial crystallography (SX) using an X-ray free-electron laser (XFEL) or synchrotron X-rays is an experimental technique that can determine the room-temperature structure of biomolecules or chemical structures [1–6]. In SX experiments, the X-ray exposure time to crystals is shorter than the X-ray exposure time to crystals in traditional X-ray cryo-crystallography, thereby minimizing the radiation damage to the crystal samples compared to that of traditional X-ray cryo-crystallography [7–9]. In particular, the room-temperature structure of macromolecules obtained using the SX technique provides more biologically relevant structural information than using traditional macromolecular cryo-crystallography in cryogenic environments [3,10,11]. In SX experiment, numerous partial diffraction information are obtained from several crystals and merged to determine the completed three-dimensional crystal structure [12]. Accordingly, the SX technique requires a large number of crystal samples compared to traditional macromolecular cryo-crystallography, which typically uses a single crystal. In addition, the SX technique requires a sample delivery system to deliver a large number of crystals to the X-ray interaction points in a stable and serial manner [13]. Various sample delivery systems, such as injectors, fixed targets, and hybrid-type sample delivery methods, have been developed for the continuous delivery of crystal samples for X-ray interactions [14]. A typical liquid-jet injector requires a high flow rate to create a stable injection stream during data collection [15]. The injection of a crystal sample embedded in a viscous medium produces a stable injection stream at a low flow rate and is widely used in synchrotron or XFEL facilities [16–18]. However, sample delivery using a viscous material requires not only the selection of a delivery material that

can stably store the crystal sample, but also technical efforts to provide a stable injection stream [16]. The fixed-target scanning method is widely applied for SX data collection at XFEL facilities or synchrotrons [19–24]. It can minimize sample consumption compared to injection systems and does not physically impact the crystal sample during data collection [25]; in the case of the injector method, pressure is applied to the crystal sample as it passes through the nozzle, which may have a physical effect on the crystal. Conversely, the FT scanning method has certain drawbacks, including dehydration and the propensity for crystals to assume a specific orientation on the sample holder. Additionally, crystal deposition on the sample holder using a pipette may impart physical damage to the crystal sample, depending on the deposition technique used.

A hybrid-type sample delivery method, such as mix-and-diffuse [26], drop-on-drop [27], a combination of an injector and fixed-target scanning [28], TapeDrive [29], and capillary-based sample delivery [30,31], is useful for reducing sample consumption. Among these various sample methods, the injector-based and hybrid-type sample delivery method requires technical handling of the injector for stable sample delivery, whereas the fixed-target scanning method only requires mounting a sample holder containing a crystal sample on a translator, without a specialized sample delivery technique. Therefore, the FT-SX experimental technique is convenient for users.

One way to minimize the consumption of crystal samples is to perform serial crystallography using pink-beam X-rays [32,33]. A pink beam has a photon flux that is substantially higher than that of the monochromatic beam and can reduce the problem of ‘partial reflection’ measurement that is inherent in the monochromatic beam [32–35]. Recently, we successfully demonstrated pink-beam serial crystallography on the beamline 1C at Pohang Light Source II (PLS-II) using a syringe-based sample delivery method [36]; however, applications using other experimental techniques have not yet been attempted. The application of pink-beam SSX using a fixed-target sample delivery method will expand the scientific program at the PLS-II 1C beamline as well as provide insights into FT-SSX experiments for other beamlines.

In this study, we performed fixed-target pink-beam serial crystallography (FT-pink-SSX) at beamline 1C at PLS-II. Herein, we introduce a newly developed magnetic-based sample holder. We collected diffraction data for glucose isomerase and lysozyme using a continuous scanning method and successfully determined their room-temperature structures. We discuss the experimental possibilities and limitations of the FT SSX experiment at 1C in PLS-II. These results will contribute to future FT pink-beam crystallography applications.

2. Materials and Methods

2.1. Protein Crystal Preparation

Glucose isomerase from *Streptomyces rubiginosus* (cat. no. HR7-102) was purchased from Hampton Research (Aliso Viejo, CA, USA). This commercial product contains crystallized glucose isomerase in a solution of 6 mM Tris-HCl, pH 7.0, 0.91 M $(\text{NH}_4)_2\text{SO}_4$, and 1 mM MgSO_4 , which is directly used for SX data collection without further purification or crystallization. The crystal suspension (50 μL) was mixed with a solution of 20 mM MgCl_2 to load the metal-binding site of the active site of glucose isomerase with magnesium ions. The size of the glucose isomerase crystal was approximately <5–300 μm , and the sample contained large- and small-sized glucose isomerase crystals.

Lysozyme isolated from chicken egg whites (cat. no. L0036) was purchased from Sigma-Aldrich (St. Louis, MO, USA). The crystallization procedure of lysozyme for the SX experiment using the batch crystallization method was the same as the method used in a previous report [36]. Briefly, the lysozyme powder (100 mg/mL) dissolved in solution containing 10 mM Tris-HCl, pH 8.0, and 200 mM NaCl was mixed with a crystallization solution containing 0.1 M Na-acetate, pH 4.4, 8% (*w/v*) polyethylene glycol 8000, and 4 M NaCl in a 1.5 mL tube. The mixture was vortexed for 30 s at 3000 rpm and incubated at 25 °C for 30 min. The size of the lysozyme crystals was approximately $20 \times 20 \times 20 \mu\text{m}^3$.

2.2. Sample Holder Preparation

A magnetic-based sample holder frame was generated by assembling eight magnets (width \times length \times depth: 5 mm \times 20 mm \times 1 mm). The outer and inner dimensions of the sample holder frame were 50 mm \times 50 mm and 40 mm \times 40 mm, respectively. The magnet of the sample holder was covered with a 300 μ m-thick PVC frame (Crenjoy, Seoul, Republic of Korea) using double-sided polyimide tape (Daehyunst, Hwasung, Republic of Korea), and a 25 μ m-thick polyimide film (Covalue Youngjin Co., Daegu, Republic of Korea) was attached to one side of the sample holder frame. We placed a nylon mesh with 70 μ m pore size (Merck, Darmstadt, Germany) in one sample holder, loaded the crystal suspension, and covered it with the other sample holder. The two sample holders were then enclosed in polyimide tape.

2.3. Data Collection

Fixed-target pink-beam SSX experiments were performed at beamline 1C at the Pohang Light Source II (PLS-II, Pohang, Republic of Korea). The pink beam was generated via the implementation of the Mo/B₄C multilayer monochromator system. The X-ray energy and energy bandwidth were 14,820 eV and 1.2% ($\Delta E/E$), respectively. The X-ray photon flux was approximately 1×10^{11} photons/s. The vertical and horizontal X-ray sizes were 130 and 100 μ m (full width at half maximum, FWHM), respectively. The fixed target sample holder was translated vertically and horizontally using 5-phase stepping motors (Tamagawa Seiki Co., Ltd., Nagano, Japan). A sample holder containing the glucose isomerase or lysozyme crystals was scanned from the top left to the bottom of the sample holder at a speed of approximately 1.786 mm/sec, then moved to the right at 400 μ m and scanned from the bottom to the top. Successive vertical scans at 400 μ m intervals covered the full area of the mesh. Diffraction data were collected at an ambient temperature (24 ± 0.4 °C). The diffraction data were recorded using a Pilatus 2M detector (Dectris, Baden-Daettwil, Switzerland). The acquisition time per diffraction pattern was 100 ms. The sample-to-detector distance was 105 mm. Diffraction images were visualized using ADXV (<https://www.scripps.edu/tainer/arvai/adxv.html>, accessed on 18 August 2023).

2.4. Data Processing

Images in which crystals were not exposed to X-rays or whose diffraction intensity was weak were filtered through the Cheetah Program [37] with the following parameters: cutoff signal/noise 5, max/min number of connected pixels 20/2, threshold 1000, and max/min number of peaks 5000/30. Diffraction images containing Bragg peaks were indexed and processed using CrystFEL v0.9.1 [38] with XGANDALF [39] or MOSFLM [40] algorithms. The geometry parameters for data processing of GI and lysozyme are shown in Supplementary Table S1. The detector geometry was optimized using a geoptimiser [41] during data processing. The reflection intensities of indexed images were scaled and merged by the partialator in the CrystFEL program [38].

2.5. Structure Determination

The phasing problem was solved by the molecular replacement method with MOL-REP [42] using the crystal structures of glucose isomerase (PDB code 7E03) [43] and lysozyme (PDB code 7E02) [43] as search models. The model was built using the COOT program [44]. Model refinement was performed using phenix.refine in PHENIX [45]. The quality of the final structures was validated using MolProbity [46]. Structural figures were generated using PyMOL (<https://pymol.org>, accessed on 18 August 2023). The superimposition of the crystal structures of glucose isomerase or lysozyme was performed using the COOT program [44].

3. Results

3.1. Experimental Setup for FT Pink-Beam SSX

We previously used a nylon mesh sample holder with a polyimide film attached to a PVC frame, which was then sealed with double-sided polyimide tape after spreading the sample onto a nylon mesh [20,21]. To minimize dehydration of the crystal suspension and increase convenience during the sample preparation procedure, we designed magnetic-based sample holders to easily enclose the protein crystals after spreading the sample on the nylon mesh on the sample holder frame (Figure 1A). The nylon mesh was installed to prevent the crystals from sinking in the crystal sample holder due to gravity. Using a combination of 5×20 mm magnets, we fabricated a sample holder frame with an inner area of 40×40 mm (Figure 1B). To install the polyimide film flatly to prevent dehydration of the crystal suspension, a 300 μ m thick PVC layer was attached to the magnet with double-sided polyimide adhesive tape. The process of spreading the crystal sample onto the nylon mesh of the sample holder and then covering it with another sample holder was the same as that reported previously [20,21]. However, the sample holder developed here could quickly cover the two sample holders without double-sided tape contact because both sample holders are magnetic (Figure 1B). Practically, the surfaces of the two sample holders are in contact with the flat PVC. In this state, even if the crystallization solution is left at room temperature for several hours, no noticeable dehydration of the solution occurs under a microscope. Nevertheless, to completely avoid evaporation of the crystallization solution, the outside of the sample holder was additionally sealed using polyimide tape.

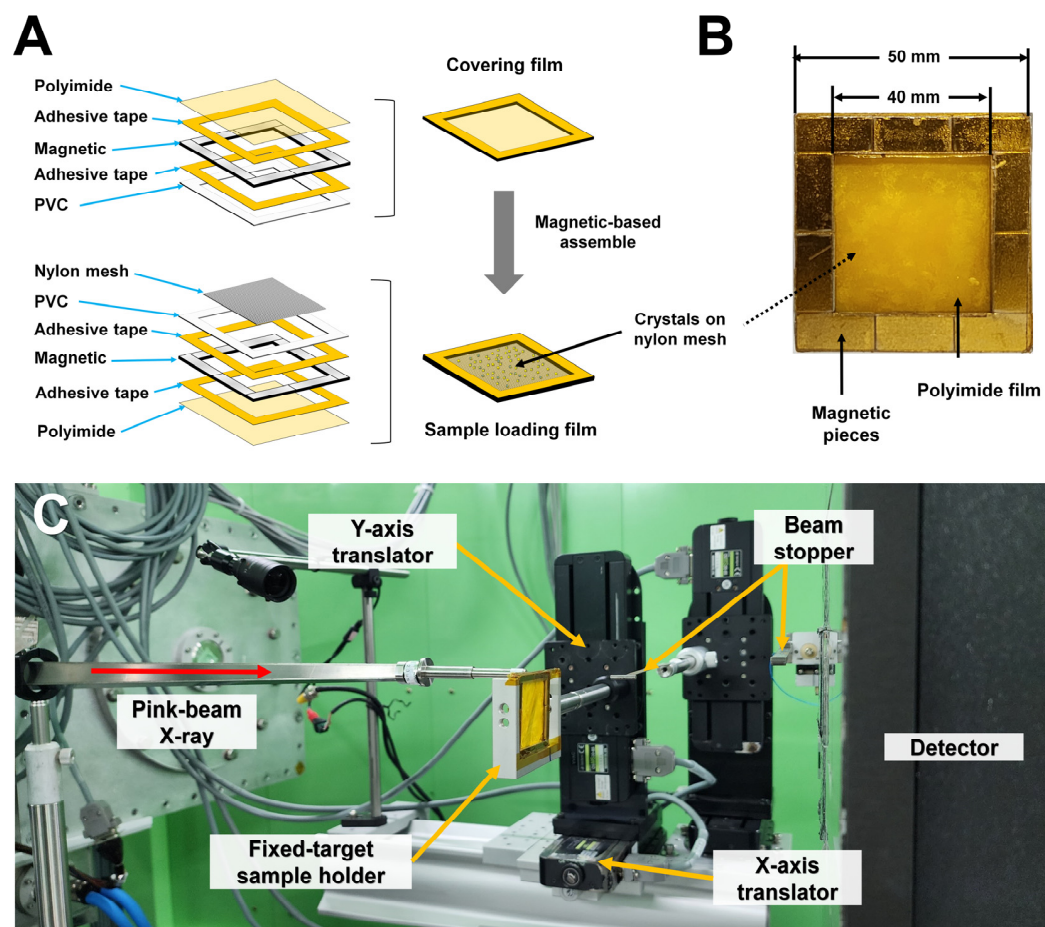


Figure 1. Experimental setup for fixed-target pink-beam serial synchrotron crystallography. (A) Preparation of the magnetic-based sample holder with nylon mesh and polyimide film. (B) Photo of a developed magnetic-based sample holder with nylon mesh. (C) Experimental setup of fixed-target pink-beam serial crystallography at 1C beamline at PLS-II.

The sample holder containing the crystal sample was mounted on a sample holder manufactured using aluminum and connected to Y translators (Figure 1C). The travel lengths of the sample holder in the horizontal and vertical directions were 85 mm and 85 mm, respectively. X-rays that had passed through the sample holder exhibited significant background, which was considered to be emitted by the X-ray halo, near the low-resolution detector. To minimize the X-ray background, the size of the X-ray beam was reduced using a slit of approximately 1 m in front of the sample position to remove all unwanted beams except for the main beam. The distance between the detector and the sample was measured using the diffraction pattern of LaB₆ powder.

3.2. FT Pink-Beam SSX Data Collection

In the early stages of FT pink-beam SSX, data collection was performed using the raster scan method. Using a stepping motor installed on the beamline, scans were performed in the vertical and horizontal directions by exposing about 50–100 ms at each scan point. Although this approach can be employed to collect SSX data, approximately 300 ms of raster scan point movement time was consumed by the stepping motor, which reduced the beam time efficiency such that more than half of the total data collection time was used to move the sample holder. To resolve this issue, we collected data by continuously moving the sample holder on the stage rather than performing a raster scan. This is different from the raster scanning approaches performed in previous SX experiments [20,21]. However, it shares a conceptual similarity with the method for continuously delivering X-ray radiation to a stream of crystals provided by an injector.

In this experiment, the translation stage moved at a speed of 1.786 mm/s in both the vertical and horizontal directions. The size of the X-ray beam was 130 μm \times 100 μm in the vertical and horizontal directions. Considering the moving speed of the translator and the X-ray beam size, the volume of all crystals was exposed within 100 ms. This X-ray exposure rate was higher than that in previous SX experiments [10,47]. However, when considering the photon number per area, less photon flux density passed through the crystal sample than in previous SX experiments. Since X-rays have a Gaussian shape profile, centrally located crystals in the 130 μm wide X-rays are exposed to more X-ray flux, while the off-center crystals are exposed to less X-ray flux. After consecutive scans in the vertical direction, the sample holder was moved by 400 μm in the horizontal direction to avoid overlapping exposure to X-rays.

A total of 20,210 and 18,959 images were collected from glucose isomerase and lysozyme data, respectively (Table 1). For the glucose isomerase data, 17,626 indexable crystals were obtained from 13,592 diffraction patterns. The multi-crystal hit rate for glucose isomerase was 22.88%. For the lysozyme data, 3485 indexable crystals were obtained from diffraction patterns. Unit-cell distributions of indexed GI and lysozyme data are shown in Supplementary Figure S1.

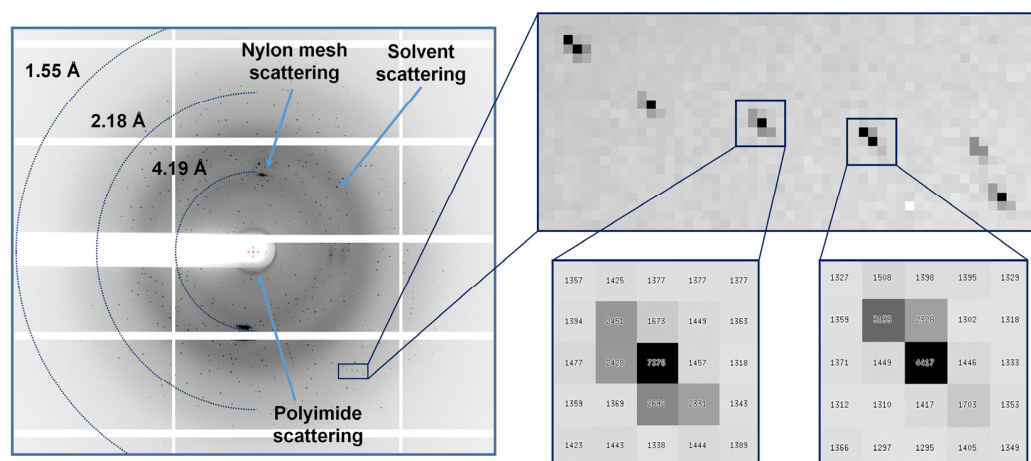
Regarding data processing, the indexing rate for lysozyme was low. This can be attributed to the substantial contamination of diffraction patterns by neighboring crystals due to the large beam size coupled with weak diffraction signals.

During glucose isomerase and lysozyme data collection, the Bragg peaks from the glucose isomerase and lysozyme data exhibited a distinctive stretched shape (Figure 2). This radial elongation phenomenon is a common feature typically encountered in mosaic crystals when employing a pink beam source [32,48]. We confirmed that multi-crystal hits were present at a high rate in the low-resolution regions of the diffraction images. The reason for the high multi-crystal hit rate in SX was the existence of a large number of protein crystals within the exposed X-ray area. In this experiment, the reason for the high multi-crystal hit rate indicates that numerous crystals were exposed using a large beam. Additionally, the large beam size is also a cause of multi-crystal hits. To reduce this, it is necessary to lower the concentration of protein crystals in the future.

Table 1. Data collection statistics.

Data Collection	Glucose Isomerase	Lysozyme
X-ray source	1C beamline, PLS-II	1C beamline, PLS-II
X-ray energy (eV)	14820	14820
X-ray exposure (ms)	100	100
Total images	20210	18959
Hit images	13592	9535
Indexed crystals	17626	3485
Space group	I222	P4 ₃ 2 ₁ 2
Cell dimension (Å)		
a, b, c	94.14, 99.94, 103.16	78.83, 78.83, 38.20
Resolution (Å)	20.00–1.70 (1.76–1.70)	20.00–2.20 (2.27–2.20)
Unique reflections	53508 (5307)	6509 (628)
Completeness (%)	100.0 (100.0)	100.0 (100.0)
Redundancy	191.5 (256.9)	488.7 (398.5)
SNR	4.67 (4.39)	5.43 (3.74)
CC	0.8239 (0.3692)	0.8737 (0.5245)
CC*	0.9505 (0.7343)	0.9657 (0.8295)
R _{split} (%)	25.98 (27.16)	21.21 (33.46)
Wilson B factor (Å ²)	11.97	23.92

Values for the outer shell are given in parentheses.

**Figure 2.** Diffraction images and close-up view of glucose isomerase from FT pink-beam SSX data.

Glucose isomerase datasets were processed up to 1.7 Å with a total of 53555 unique reflections. The overall completeness, SNR, CC, CC*, and R_{split} values were 100, 4.67, 0.8240, 0.9505, and 25.98, respectively (Table 1). Lysozyme datasets were processed up to 2.2 Å with a total of 6525 unique reflections. The overall completeness, SNR, CC, CC*, and R_{split} values were 100, 5.43, 0.8741, 0.9658, and 5.43, respectively (Table 1). All data collection statistics for glucose isomerase and lysozyme were sufficient to determine the crystal structure, but the CC values were relatively poor compared to other parameters. Although the CC* value in the last shell, especially for lysozyme, appears high, it is essential to note that the resolution cutoff was comprehensively determined considering both the CC and R_{free} values after the final structure refinement process.

3.3. Structure Determination

Crystal structures of glucose isomerase and lysozyme were determined at 1.7 and 2.2 Å resolution, respectively (Table 2). During refinement, the low-resolution area (beam stopper ~7 Å) data containing an X-ray background were not used to generate better R-values. The values of R_{work}/R_{free} for glucose isomerase and lysozyme were 25.10/27.79 and 25.12/29.93, respectively. These R-values are suitable for the representation of the model structure but are not as good as the previous result. The structures we determined in

this study exhibited relatively elevated R-values. Our ongoing investigations are centered on discerning the root causes of this phenomenon, which may be attributed to factors such as insufficient data volume, heightened background scattering, or quality degradation stemming from multi-crystal hits. Addressing these factors can contribute to improving the overall quality of the data.

Table 2. Data refinement statistics.

Refinement	Glucose Isomerase	Lysozyme
Resolution (Å)	7.0–1.7	7.0–2.2
$R_{\text{work}}^{\text{a}}$	0.2510	0.2512
$R_{\text{free}}^{\text{b}}$	0.2779	0.2993
R.m.s. deviations		
Bonds (Å)	0.004	0.008
Angles (°)	0.861	0.969
B factors (Å ²)		
Protein	13.42	12.11
Water	7.58	16.24
Ramachandran plot (%)		
Favored	93.46	95.28
Allowed	5.76	4.72
Disallowed	0.79	0.00

^a $R_{\text{work}} = \frac{\sum ||\text{Fobs}| - |\text{Fcalc}||}{\sum |\text{Fobs}|}$, where Fobs and Fcalc are the observed and calculated structure factor amplitudes, respectively. ^b R_{free} was calculated as R_{work} using a randomly selected subset (10%) of unique reflections not used for structural refinement.

The electron density map of glucose isomerase was well-ordered to trace the amino acids from Tyr3 to Arg387 (Figure 3A). Glucose isomerase contains two metal-binding active sites that are involved in substrate-binding and catalytic reactions [49]. Commercially available glucose isomerases often have no metal or low occupancy at the M2 site; therefore, Mg^{2+} was added to obtain the functional two-metal-bound glucose isomerase structure before data collection. Interestingly, the M1 metal ion was coordinated to Asp181, Glu217, Asp245, and Asp287, whereas the M2 metal ion was coordinated to Glu217, Asp255, and Asp257. These functional metal-binding coordinations at M1 and M2 are identical to those observed in previous glucose isomerase structures, excluding the position of the His220 residue, which was different. High-Z atoms are more sensitive to radiation damage than low-Z atoms [50]. Electron density map analysis showed no significant radiation damage at the two metal ion-binding sites of glucose isomerase (Figure 3B). The B-factor values of the M1 and M2 metal-binding sites were 2.24 and 2.50 Å², respectively, which is lower than the average B-factor of whole amino acids of 13.42 Å².

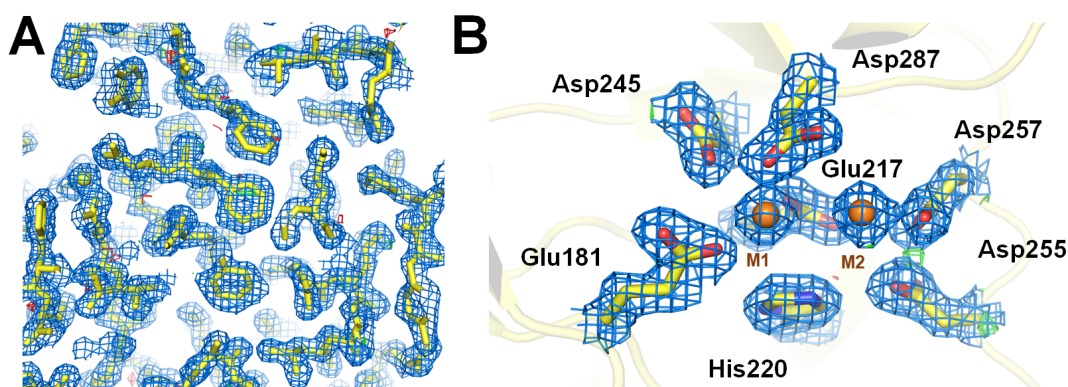


Figure 3. Room-temperature structure of glucose isomerase determined by FT pink-beam SSX. 2mFo-DFc (blue, 1.0 σ) and mFo-DFc (green, 3.0 σ and red, -3.0σ) electron density map of (A) glucose isomerase and (B) close-up view of metal binding sites at active site of glucose isomerase.

The room-temperature structure of glucose isomerase determined in this study was similar to the previously reported room-temperature structure of glucose isomerase (PDB codes: 7E03) [43] determined using SX techniques, with an r.m.s. deviation of 0.275 Å–0.275 Å.

The electron density map of lysozyme was well-ordered to trace the amino acids from Lys19 to Leu147 (Figure 4A). The side chains of the active site region of lysozyme were clearly observed, excluding long side chains such as Arg and Glu. Lysozyme contains four disulfide bonds (Cys24–Cys145, Cys48–Cys133, Cys82–Cys98, and Cys94–Cys112) that are useful for interpreting X-ray radiation damage. The electron density map showed no significant radiation damage at any disulfide bond in the lysozyme (Figure 4B). The room-temperature structure of lysozyme determined in this study was similar to the previously reported room-temperature structure of lysozyme (PDB codes: 7CVJ) [21] determined using SX techniques, with an r.m.s. deviation of 0.153 Å.

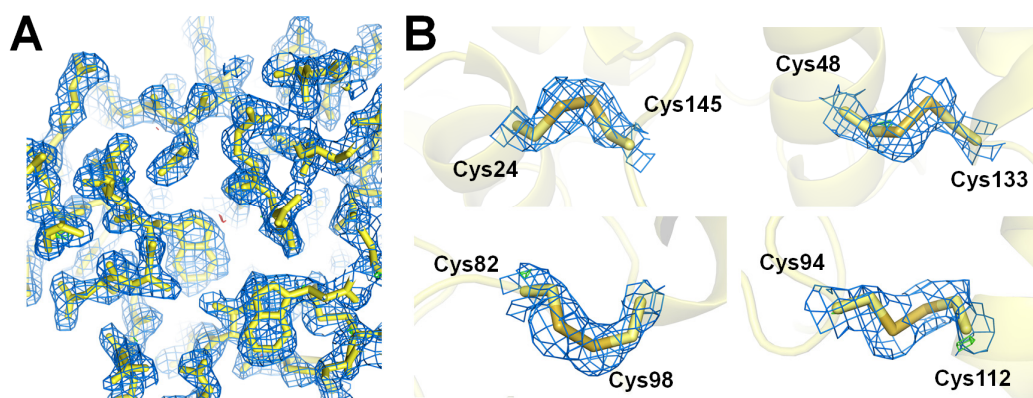


Figure 4. Room-temperature of lysozyme determined by FT-pink-beam SSX. 2mFo-DFc (blue, 1.0 σ) and mFo-DFc (green, 3.0 σ and red, -3.0 σ) electron density map of (A) lysozyme and (B) close-up view of disulfide bonds of lysozyme.

4. Discussion

In general, when a pink-beam SSX experiment is performed rather than an SX experiment using a monochromatic beam in a synchrotron, sample consumption can be reduced, and data with higher diffraction intensity can be collected compared to monochromatic beams [32–34]. We previously demonstrated a pink-beam SSX experiment at beamline 1C at PLS-II using a syringe with a viscous medium [36]. Here, pink-beam SSX experiments at beamline 1C of the PLS-II were performed using an FT scanning method that can reduce sample consumption compared to the injection method.

In this study, we used a newly developed magnetic-based sample holder. This sample holder enables simpler sample preparation than that of the previous sample holder that used double-sided adhesive tape [20,21] because the two sample chips are attached by two magnets. When the magnetic-based sample holder containing the crystals was left at room temperature for several hours, no significant dehydration of the crystallization solution was observed under the microscope. It is judged that there is no space for the crystallization solution to escape because of the contact between the magnet and the flat PVC plate or that the solution does not escape through fine gaps owing to surface tension and is stable inside. Although we confirmed that evaporation of the solution is not a problem through preliminary testing, additional polyimide tape was used to seal it perfectly and can be used in place of other materials such as grease. Previous nylon-mesh-based sample holders fixed the two sample holders with double-sided tape [20,21], so it was difficult to remove the double-sided tape and attach it again for reuse. However, the magnetic-based sample holder developed here was maintained by the magnets on the contact surfaces of the two sample holders; therefore, it could be reused immediately after washing the sample holder following the data collection experiment. In this experimental setup, considering the crystal size of glucose isomerase and lysozyme, mounting was performed using a nylon mesh with a pore size of 70 μm . The choice of nylon mesh pore size can vary depending

on the size of the target crystal samples. The overall thickness of the polyimide film in the sample holder used in this experiment was 50 μm . Notably, we did not encounter any notable issues related to X-ray background scattering caused by the polyimide films when processing data for glucose isomerase and lysozyme model samples. However, it is essential to acknowledge that employing thinner films in the sample holder can lead to reduced background scattering, thereby potentially enhancing the quality of the collected data. Meanwhile, a pink beam exhibits relatively high background scattering compared to a monochromatic beam [32]. In SX utilizing a pink-beam, enhancing data quality can be achieved by mitigating background scattering through methods like capillary beamstop or X-ray focusing, which reduce air scattering [32].

During glucose isomerase and lysozyme data collection, multi-crystal hits had a high presence rate in the low-resolution regions of the diffraction images. When the same crystal sample distributed in the same area is scanned with the micro-focusing beam, the multi-crystal hit rate in the micro-focusing beam will be low, while the photon flux density exposed to the crystal sample will be high. Conversely, when a large X-ray beam is used, more crystals are exposed compared to the micro-focusing beam, resulting in a higher multi-crystal hit rate and providing a relatively low photon flux density to the crystal sample. In this respect, during SX data collection, it is advantageous to increase the quality of the data using the micro-focusing beam rather than the large beam used in this experiment. However, micro-focusing beams are not available on all beamlines and installing micro-focusing optics on existing beamlines requires considerable time and effort. Accordingly, when employing a fixed target in an SX experiment using a large beam, a strategy different from that of the existing micro-focusing beamline is required. When performing FT-SX using a large beam, the multi-crystal hit rate can be controlled by reducing the concentration of the sample, which can increase the indexing efficiency and improve the SNR quality during data processing. A large beam provides lower photon flux to the same area as a micro-focused beam. One way to solve this problem is to increase the photon flux to the crystal sample by increasing the X-ray exposure time. However, this has the disadvantage of increasing the data collection time. Nevertheless, this data collection will be helpful for other applications in SSX experiments using large beam sizes at other beamlines or synchrotrons. Currently, the 1C beamline has not planned the installation of microfocus optics, such as KB mirrors; therefore, a long X-ray beamtime is required to collect FT pink-beam SSX data.

In summary, we demonstrated fixed-target pink-beam serial synchrotron crystallography at the Pohang Light Source II. We report a newly developed magnetic-based sample holder and determine the room-temperature structures of glucose isomerase and lysozyme. We discuss the possibilities and limitations of a fixed-target pink-beam SSX using a large X-ray beam. This result will be useful for further data collection strategies for FT-SSX at the 1C beamline of PAL-II and other beamlines using a large X-ray beam.

Supplementary Materials: The following supporting information can be downloaded at: <https://www.mdpi.com/article/10.3390/cryst13111544/s1>, Figure S1: Distribution of unit cell parameters resulting from glucose isomerase and lysozyme diffraction patterns; Table S1: Detector geometry parameter for data processing.

Author Contributions: Conceptualization: K.H.N.; methodology: Y.K. and K.H.N.; software: Y.K. and K.H.N.; validation: K.H.N.; formal analysis: K.H.N.; investigation: K.H.N.; data curation: Y.K. and K.H.N.; writing—original draft preparation: K.H.N.; writing—review and editing: Y.K.; visualization: K.H.N.; funding acquisition: K.H.N. All authors have read and agreed to the published version of the manuscript.

Funding: This work was funded by the National Research Foundation of Korea (NRF) (NRF-2017M3A9F6029736 and NRF-2021R111A1A01050838) and Korea Initiative for Fostering University of Research and Innovation (KIURI) Program of the NRF (NRF-2020M3H1A1075314). This study was supported by ProGen.

Institutional Review Board Statement: Not applicable.

Informed Consent Statement: Not applicable.

Data Availability Statement: Diffraction images and geometry files have been deposited in Zenodo under the accession <https://doi.org/10.5281/zenodo.8347473> (accessed on 18 August 2023) (glucose isomerase) and <https://doi.org/10.5281/zenodo.8354296> (accessed on 18 August 2023) (lysozyme). The structure factors and coordinates have been deposited in the Protein Data Bank under the accession codes 8WDH (glucose isomerase) and 8WDI (lysozyme).

Acknowledgments: We would like to thank the beamline staff at the 1C beamline at the Pohang Accelerator Laboratory for their assistance with data collection. Experiments at the 1C beamline, PLS-II, were supported by MSIT and the Global Science Experimental Data Hub Center (GSDC) at the Korea Institute of Science and Technology Information (KISTI) provided computational support.

Conflicts of Interest: The authors declare no conflict of interest.

References

1. Chapman, H.N.; Fromme, P.; Barty, A.; White, T.A.; Kirian, R.A.; Aquila, A.; Hunter, M.S.; Schulz, J.; DePonte, D.P.; Weierstall, U.; et al. Femtosecond X-ray protein nanocrystallography. *Nature* **2011**, *470*, 73–77. [[CrossRef](#)] [[PubMed](#)]
2. Chapman, H.N.; Caleman, C.; Timneanu, N. Diffraction before destruction. *Philos. Trans. R. Soc. Lond. B Biol. Sci.* **2014**, *369*, 20130313. [[CrossRef](#)]
3. Boutet, S.; Lomb, L.; Williams, G.J.; Barends, T.R.M.; Aquila, A.; Doak, R.B.; Weierstall, U.; DePonte, D.P.; Steinbrener, J.; Shoeman, R.L.; et al. High-Resolution Protein Structure Determination by Serial Femtosecond Crystallography. *Science* **2012**, *337*, 362–364. [[CrossRef](#)] [[PubMed](#)]
4. Durdagi, S.; Dag, C.; Dogan, B.; Yigin, M.; Avsar, T.; Buyukdag, C.; Erol, I.; Ertem, F.B.; Calis, S.; Yildirim, G.; et al. Near-physiological-temperature serial crystallography reveals conformations of SARS-CoV-2 main protease active site for improved drug repurposing. *Structure* **2021**, *29*, 1382–1396. [[CrossRef](#)] [[PubMed](#)]
5. Schriber, E.A.; Paley, D.W.; Bolotovskiy, R.; Rosenberg, D.J.; Sierra, R.G.; Aquila, A.; Mendez, D.; Poitevin, F.; Blaschke, J.P.; Bhowmick, A.; et al. Chemical crystallography by serial femtosecond X-ray diffraction. *Nature* **2022**, *601*, 360–365. [[CrossRef](#)]
6. Takaba, K.; Maki-Yonekura, S.; Inoue, I.; Tono, K.; Hamaguchi, T.; Kawakami, K.; Naitow, H.; Ishikawa, T.; Yabashi, M.; Yonekura, K. Structural resolution of a small organic molecule by serial X-ray free-electron laser and electron crystallography. *Nat. Chem.* **2023**, *15*, 491–497. [[CrossRef](#)]
7. Grünbein, M.L.; Nass Kovacs, G. Sample delivery for serial crystallography at free-electron lasers and synchrotrons. *Acta Crystallogr. D Biol. Crystallogr.* **2019**, *75*, 178–191. [[CrossRef](#)]
8. Martiel, I.; Muller-Werkmeister, H.M.; Cohen, A.E. Strategies for sample delivery for femtosecond crystallography. *Acta Crystallogr. D Struct. Biol.* **2019**, *75*, 160–177. [[CrossRef](#)]
9. Shelley, K.L.; Garman, E.F. Quantifying and comparing radiation damage in the Protein Data Bank. *Nat. Commun.* **2022**, *13*, 1314. [[CrossRef](#)]
10. Weinert, T.; Olieric, N.; Cheng, R.; Brunle, S.; James, D.; Ozerov, D.; Gashi, D.; Vera, L.; Marsh, M.; Jaeger, K.; et al. Serial millisecond crystallography for routine room-temperature structure determination at synchrotrons. *Nat. Commun.* **2017**, *8*, 542. [[CrossRef](#)]
11. Pearson, A.R.; Mehrabi, P. Serial synchrotron crystallography for time-resolved structural biology. *Curr. Opin. Struct. Biol.* **2020**, *65*, 168–174. [[CrossRef](#)] [[PubMed](#)]
12. White, T.A.; Barty, A.; Stellato, F.; Holton, J.M.; Kirian, R.A.; Zatsepin, N.A.; Chapman, H.N. Crystallographic data processing for free-electron laser sources. *Acta Crystallogr. D Biol. Crystallogr.* **2013**, *69*, 1231–1240. [[CrossRef](#)]
13. Zhao, F.Z.; Zhang, B.; Yan, E.K.; Sun, B.; Wang, Z.J.; He, J.H.; Yin, D.C. A guide to sample delivery systems for serial crystallography. *FEBS J.* **2019**, *286*, 4402–4417. [[CrossRef](#)] [[PubMed](#)]
14. Sierra, R.G.; Weierstall, U.; Oberthuer, D.; Sugahara, M.; Nango, E.; Iwata, S.; Meents, A. Sample Delivery Techniques for Serial Crystallography. In *X-ray Free Electron Lasers*; Springer: Cham, Switzerland, 2018; pp. 109–184. [[CrossRef](#)]
15. DePonte, D.P.; Weierstall, U.; Schmidt, K.; Warner, J.; Starodub, D.; Spence, J.C.H.; Doak, R.B. Gas dynamic virtual nozzle for generation of microscopic droplet streams. *J. Phys. D* **2008**, *41*, 195505. [[CrossRef](#)]
16. Nam, K.H. Sample delivery media for serial crystallography. *Int. J. Mol. Sci.* **2019**, *20*, 1094. [[CrossRef](#)]
17. Weierstall, U.; James, D.; Wang, C.; White, T.A.; Wang, D.; Liu, W.; Spence, J.C.; Bruce Doak, R.; Nelson, G.; Fromme, P.; et al. Lipidic cubic phase injector facilitates membrane protein serial femtosecond crystallography. *Nat. Commun.* **2014**, *5*, 3309. [[CrossRef](#)] [[PubMed](#)]
18. Sugahara, M.; Mizohata, E.; Nango, E.; Suzuki, M.; Tanaka, T.; Masudala, T.; Tanaka, R.; Shimamura, T.; Tanaka, Y.; Suno, C.; et al. Grease matrix as a versatile carrier of proteins for serial crystallography. *Nat. Methods* **2015**, *12*, 61–63. [[CrossRef](#)] [[PubMed](#)]
19. Hunter, M.S.; Segelke, B.; Messerschmidt, M.; Williams, G.J.; Zatsepin, N.A.; Barty, A.; Benner, W.H.; Carlson, D.B.; Coleman, M.; Graf, A.; et al. Fixed-target protein serial microcrystallography with an X-ray free electron laser. *Sci. Rep.* **2014**, *4*, 6026. [[CrossRef](#)]
20. Lee, D.; Baek, S.; Park, J.; Lee, K.; Kim, J.; Lee, S.J.; Chung, W.K.; Lee, J.L.; Cho, Y.; Nam, K.H. Nylon mesh-based sample holder for fixed-target serial femtosecond crystallography. *Sci. Rep.* **2019**, *9*, 6971. [[CrossRef](#)]

21. Park, S.Y.; Choi, H.; Eo, C.; Cho, Y.; Nam, K.H. Fixed-target serial synchrotron crystallography using nylon mesh and enclosed film-based sample holder. *Crystals* **2020**, *10*, 803. [[CrossRef](#)]
22. Tolstikova, A.; Levantino, M.; Yefanov, O.; Hennicke, V.; Fischer, P.; Meyer, J.; Mozzanica, A.; Redford, S.; Crosas, E.; Opara, N.L.; et al. 1 kHz fixed-target serial crystallography using a multilayer monochromator and an integrating pixel detector. *IUCr* **2019**, *6*, 927–937. [[CrossRef](#)] [[PubMed](#)]
23. Gu, K.K.; Liu, Z.; Narayanasamy, S.R.; Shelby, M.L.; Chan, N.; Coleman, M.A.; Frank, M.; Kuhl, T.L. All polymer microfluidic chips—A fixed target sample delivery workhorse for serial crystallography. *Biomicrofluidics* **2023**, *17*, 051302. [[CrossRef](#)]
24. Bjelčić, M.; Sigfridsson Clauss, K.G.V.; Aurelius, O.; Milas, M.; Nan, J.; Ursby, T. Anaerobic fixed-target serial crystallography using sandwiched silicon nitride membranes. *Acta Crystallogr. D Biol. Crystallogr.* **2023**, *79*. [[CrossRef](#)] [[PubMed](#)]
25. Oghbaey, S.; Sarracini, A.; Ginn, H.M.; Pare-Labrosse, O.; Kuo, A.; Marx, A.; Epp, S.W.; Sherrell, D.A.; Eger, B.T.; Zhong, Y.; et al. Fixed target combined with spectral mapping: Approaching 100% hit rates for serial crystallography. *Acta Crystallogr. D Struct. Biol.* **2016**, *72*, 944–955. [[CrossRef](#)]
26. Beyerlein, K.R.; Dierksmeyer, D.; Mariani, V.; Kuhn, M.; Sarrou, I.; Ottaviano, A.; Awel, S.; Knoska, J.; Fuglerud, S.; Jonsson, O.; et al. Mix-and-diffuse serial synchrotron crystallography. *IUCr* **2017**, *4*, 769–777. [[CrossRef](#)] [[PubMed](#)]
27. Butryn, A.; Simon, P.S.; Aller, P.; Hinchliffe, P.; Massad, R.N.; Leen, G.; Tooke, C.L.; Bogacz, I.; Kim, I.S.; Bhowmick, A.; et al. An on-demand, drop-on-drop method for studying enzyme catalysis by serial crystallography. *Nat. Commun.* **2021**, *12*, 4461. [[CrossRef](#)]
28. Lee, K.; Kim, J.; Baek, S.; Park, J.; Park, S.; Lee, J.-L.; Chung, W.K.; Cho, Y.; Nam, K.H. Combination of an inject-and-transfer system for serial femtosecond crystallography. *J. Appl. Crystallogr.* **2022**, *55*, 813–822. [[CrossRef](#)]
29. Zielinski, K.A.; Prester, A.; Andaleeb, H.; Bui, S.; Yefanov, O.; Catapano, L.; Henkel, A.; Wiedorn, M.O.; Lorbeer, O.; Crosas, E.; et al. Rapid and efficient room-temperature serial synchrotron crystallography using the CFEL TapeDrive. *IUCr* **2022**, *9*, 778–791. [[CrossRef](#)]
30. Stellato, F.; Oberthür, D.; Liang, M.; Bean, R.; Gati, C.; Yefanov, O.; Barty, A.; Burkhardt, A.; Fischer, P.; Galli, L.; et al. Room-temperature macromolecular serial crystallography using synchrotron radiation. *IUCr* **2014**, *1*, 204–212. [[CrossRef](#)]
31. Ghosh, S.; Zorić, D.; Dahl, P.; Bjelčić, M.; Johannesson, J.; Sandelin, E.; Borjesson, P.; Björling, A.; Banacore, A.; Edlund, P.; et al. A simple goniometer-compatible flow cell for serial synchrotron X-ray crystallography. *J. Appl. Crystallogr.* **2023**, *56*, 449–460. [[CrossRef](#)]
32. Meents, A.; Wiedorn, M.O.; Srajer, V.; Henning, R.; Sarrou, I.; Bergtholdt, J.; Barthelmess, M.; Reinke, P.Y.A.; Dierksmeyer, D.; Tolstikova, A.; et al. Pink-beam serial crystallography. *Nat. Commun.* **2017**, *8*, 1281. [[CrossRef](#)] [[PubMed](#)]
33. Martin-Garcia, J.M.; Zhu, L.; Mendez, D.; Lee, M.-Y.; Chun, E.; Li, C.; Hu, H.; Subramanian, G.; Kissick, D.; Ogata, C.; et al. High-viscosity injector-based pink-beam serial crystallography of microcrystals at a synchrotron radiation source. *IUCr* **2019**, *6*, 412–425. [[CrossRef](#)]
34. Dejoie, C.; McCusker, L.B.; Baerlocher, C.; Abela, R.; Patterson, B.D.; Kunz, M.; Tamura, N. Using a non-monochromatic microbeam for serial snapshot crystallography. *J. Appl. Crystallogr.* **2013**, *46*, 791–794. [[CrossRef](#)]
35. Nakane, T. Pink beam crystallography demonstrated in SFX. *IUCr* **2021**, *8*, 853–854. [[CrossRef](#)] [[PubMed](#)]
36. Kim, Y.; Nam, K.H. Pink-Beam Serial Synchrotron Crystallography at Pohang Light Source II. *Crystals* **2022**, *12*, 1637. [[CrossRef](#)]
37. Barty, A.; Kirian, R.A.; Maia, F.R.; Hantke, M.; Yoon, C.H.; White, T.A.; Chapman, H. Cheetah: Software for high-throughput reduction and analysis of serial femtosecond X-ray diffraction data. *J. Appl. Crystallogr.* **2014**, *47*, 1118–1131. [[CrossRef](#)] [[PubMed](#)]
38. White, T.A.; Mariani, V.; Brehm, W.; Yefanov, O.; Barty, A.; Beyerlein, K.R.; Chervinskii, F.; Galli, L.; Gati, C.; Nakane, T.; et al. Recent developments in CrystFEL. *J. Appl. Crystallogr.* **2016**, *49*, 680–689. [[CrossRef](#)]
39. Gevorkov, Y.; Yefanov, O.; Barty, A.; White, T.A.; Mariani, V.; Brehm, W.; Tolstikova, A.; Grigat, R.R.; Chapman, H.N. XGANDALF—Extended gradient descent algorithm for lattice finding. *Acta Crystallogr. A Found. Adv.* **2019**, *75*, 694–704. [[CrossRef](#)]
40. Battye, T.G.; Kontogiannis, L.; Johnson, O.; Powell, H.R.; Leslie, A.G. iMOSFLM: A new graphical interface for diffraction-image processing with MOSFLM. *Acta Crystallogr. D Biol. Crystallogr.* **2011**, *67*, 271–281. [[CrossRef](#)]
41. Yefanov, O.; Mariani, V.; Gati, C.; White, T.A.; Chapman, H.N.; Barty, A. Accurate determination of segmented X-ray detector geometry. *Opt. Express* **2015**, *23*, 28459–28470. [[CrossRef](#)]
42. Vagin, A.; Teplyakov, A. Molecular replacement with MOLREP. *Acta Crystallogr. D Biol. Crystallogr.* **2010**, *66*, 22–25. [[CrossRef](#)] [[PubMed](#)]
43. Nam, K.H. Beef tallow injection matrix for serial crystallography. *Sci. Rep.* **2022**, *12*, 694. [[CrossRef](#)] [[PubMed](#)]
44. Emsley, P.; Cowtan, K. Coot: Model-building tools for molecular graphics. *Acta Crystallogr. D Biol. Crystallogr.* **2004**, *60*, 2126–2132. [[CrossRef](#)] [[PubMed](#)]
45. Liebschner, D.; Afonine, P.V.; Baker, M.L.; Bunkoczi, G.; Chen, V.B.; Croll, T.I.; Hintze, B.; Hung, L.W.; Jain, S.; McCoy, A.J.; et al. Macromolecular structure determination using X-rays, neutrons and electrons: Recent developments in Phenix. *Acta Crystallogr. D Struct. Biol.* **2019**, *75*, 861–877. [[CrossRef](#)]
46. Williams, C.J.; Headd, J.J.; Moriarty, N.W.; Prisant, M.G.; Videau, L.L.; Deis, L.N.; Verma, V.; Keedy, D.A.; Hintze, B.J.; Chen, V.B.; et al. MolProbity: More and better reference data for improved all-atom structure validation. *Protein Sci.* **2018**, *27*, 293–315. [[CrossRef](#)]

47. Martin-Garcia, J.M.; Conrad, C.E.; Nelson, G.; Stander, N.; Zatsepin, N.A.; Zook, J.; Zhu, L.; Geiger, J.; Chun, E.; Kissick, D.; et al. Serial millisecond crystallography of membrane and soluble protein microcrystals using synchrotron radiation. *IUCrJ* **2017**, *4*, 439–454. [[CrossRef](#)]
48. Andrews, S.J.; Hails, J.E.; Harding, M.M.; Cruickshank, D.W.J. The mosaic spread of very small crystals deduced from Laue diffraction patterns. *Acta Crystallogr. A Found. Adv.* **1987**, *43*, 70–73. [[CrossRef](#)]
49. Bhosale, S.H.; Rao, M.B.; Deshpande, V.V. Molecular and industrial aspects of glucose isomerase. *Microbiol. Rev.* **1996**, *60*, 280–300. [[CrossRef](#)]
50. Gopakumar, G.; Unger, I.; Slavíček, P.; Hergenbahn, U.; Öhrwall, G.; Malerz, S.; Céolin, D.; Trinter, F.; Winter, B.; Wilkinson, I.; et al. Radiation damage by extensive local water ionization from two-step electron-transfer-mediated decay of solvated ions. *Nat. Chem.* **2023**, *15*, 1408–1414. [[CrossRef](#)]

Disclaimer/Publisher’s Note: The statements, opinions and data contained in all publications are solely those of the individual author(s) and contributor(s) and not of MDPI and/or the editor(s). MDPI and/or the editor(s) disclaim responsibility for any injury to people or property resulting from any ideas, methods, instructions or products referred to in the content.